

The BSS population in NGC 6229^{*}

N. Sanna^{1,2,†}, E. Dalessandro¹, B. Lanzoni¹, F.R. Ferraro¹, G. Beccari³, R.T. Rood²

¹*Dipartimento di Astronomia, Università degli Studi di Bologna, via Ranzani 1, I-40127 Bologna, Italy*

²*Astronomy Department, University of Virginia, P.O. Box 400325, Charlottesville, VA, 22904*

³*European Southern Observatory, Karl-Schwarzschild-Str. 2, D-85748 Garching bei Munchen, Germany*

7 February 2012

ABSTRACT

We have used a combination of high-resolution *Hubble Space Telescope* WFPC2 and wide-field ground-based observations in ultraviolet and optical bands to study the blue straggler star (BSS) population of the outer-halo globular cluster NGC 6229, over its entire radial extent. A total of 64 bright BSS (with $m_{255} \leq 21.30$, corresponding to $m_{555} \leq 20.75$) has been identified. The BSS projected radial distribution is found to be bimodal, with a high central peak, a well defined minimum at intermediate radii ($r \sim 40''$), and an upturn in the outskirts. From detailed star counts even in the very inner region, we compute the centre of gravity of the cluster and the most accurate and extended radial density profile ever published for this system. The profile is reasonably well reproduced by a standard King model with an extended core ($r_c \simeq 9.5''$) and a modest value of the concentration parameter ($c \simeq 1.49$). However, a deviation from the model is noted in the most external region of the cluster (at $r > 250''$ from the centre). This feature needs to be further investigated in order to assess the possible presence of a tidal tail in this cluster.

Key words: Globular clusters: individual (NGC 6229); stars: evolution - binaries: general - blue stragglers

1 INTRODUCTION

In the optical colour-magnitude diagram (CMD) of globular clusters (GCs) the so called blue stragglers stars (BSS) are bluer and brighter than the main sequence (MS) objects, appearing younger and more massive than the normal cluster stars (as also confirmed by direct mass measurements, e.g. Shara et al. 1997). Indeed the BSS mass distribution in 47 Tucanae (47 Tuc) and in NGC 1904, derived from the star position in the CMD, has been found to peak between 1.1 and 1.2 M_\odot (see Ferraro et al. 2006a, Lanzoni et al. 2007a). This suggests that BSS increase their initial mass during their evolution. Possible explanations involve the secular (or induced) evolution of primordial binary systems and collisions between single and/or binary stars (hereafter PB-BSS

and COL-BSS, respectively; see McCrea 1964, e.g. Bailyn 1995, Sills et al. 1997, and references therein).

Promising chemical and photometric signatures of different BSS formation mechanisms have been recently found. In 47 Tuc Ferraro et al. (2006a) discovered a subpopulation of BSS showing a significant depletion of carbon and oxygen, possibly due to a formation through mass transfer activity in PB-BSS. In M30 two distinct sequences of BSS have been discovered by Ferraro et al. (2009). The authors argued that they are populated by BSS originated by the two formation channels, both triggered by the collapse of the cluster core a few Gyr ago.

In many GCs (M3, 47 Tuc, NGC 6752, M5, M55, NGC 6388, M53, M2, all references in Beccari et al. 2008; Dalessandro et al. 2008a,b, 2009) the projected radial distribution of BSS has been found to be bimodal: highly peaked in the centre, with a clear-cut dip at intermediate radii, and with an upturn in the external regions. Dynamical simulations (Mapelli et al. 2004, 2006; Lanzoni et al. 2007a,b) suggest that the observed central peak is due to COL-BSS formed in the core and/or PB-BSS sunk into the centre because of dynamical friction, while the external rising branch is made of PB-BSS evolving in isolation in the cluster outskirts. NGC 1904 (Lanzoni et al. 2007a) and M75 (Contreras Ramos et al. 2012) do not show any bimodality, but BSS appear more segregated in the central regions than the ref-

^{*} Based on observations with the NASA/ESA *HST* (Prop. 11975), obtained at the Space Telescope Science Institute, which is operated by AURA, Inc., under NASA contract NAS5-26555. Also based on observations with MegaPrime/MegaCam, a joint project of CFHT and CEA/DAPNIA, at the Canada-France-Hawaii Telescope (CFHT), which is operated by the National Research Council (NRC) of Canada, the Institut National des Sciences de l'Univers of the Centre National de la Recherche Scientifique of France, and the University of Hawaii.

[†] E-mail: nicoletta.sanna2@unibo.it

erence cluster stars. In only three cases (ω Centauri, Ferraro et al. 2006b; NGC 2419, Dalessandro et al. 2008b; Pal 14, Beccari et al. 2011), the radial distribution of BSS is indistinguishable from that of the other stars, suggesting that these clusters are not significantly mass-segregated yet.

This paper is part of a series devoted to study the UV bright populations (including horizontal branch -HB, BSS and post-asymptotic giant branch stars), in old stellar clusters, by means of an extensive survey conducted with the Wide Field Planetary Camera 2 (WFPC2) on board the *Hubble Space Telescope* (HST). More than 30 Galactic GCs have been observed within this project. Here we present a detailed analysis of the BSS population in NGC 6229. This is one of the most remote GC associated to outer halo of the Galaxy, located at ~ 31 kpc from the Galactic centre (Ferraro et al. 1999). It probably is a Magellanic Stream member (Palma et al. 2002) and due to its location, it is poorly studied. The most recent papers are focused on HB stars (Borissova et al. 1997, 1999, Catelan et al. 1998), BSS (Borissova et al. 1999), and variable stars (Borissova et al. 2001). However, these papers are based on ground-based observations only, while here we present a study that combines high-resolution observations from space, thus to properly explore, for the very first time, the stellar populations in the cluster core, and wide-field observations from the ground to study the entire cluster extension.

The paper is organized as follows. Section 2 describes the data set and the photometric and astrometric analysis. In Section 3 we determine the centre of gravity and present the CMDs. The radial density profile of the cluster is discussed in Section 4. In Section 5 we discuss the BSS properties and present our conclusions. The summary of the paper is presented in Section 6.

2 OBSERVATIONS AND DATA ANALYSIS

In order both to resolve the stars in the crowded central regions, and to cover the entire extension of the cluster, we used a combination of high-resolution and wide-field data, similarly to what already done in our previous studies (e.g. Dalessandro et al. 2009 and references therein). The *high-resolution set* consists of a series of images collected with the HST/WFPC2 at various wavelengths, ranging from the UV to the optical bands. These images (Prop. 11975, P.I. Ferraro) were obtained through the UV filter $F255W$ with total exposure times $t_{\text{exp}} = 3600$ s, and through the optical filters $F336W$ and $F555W$ with exposure times $t_{\text{exp}} = 3000$ s and $t_{\text{exp}} = 245$ s, respectively. The centre of the cluster is located in the Planetary Camera (PC, pixel scale $\sim 0.05''$ pixel $^{-1}$). The *wide-field set* is composed of data obtained with the MegaCam on the Canada-France-Hawaii Telescope (CFHT). A series of 11 images taken through the g' and r' filters with total exposure times $t_{\text{exp}} = 450$ s and $t_{\text{exp}} = 540$ s, respectively, was retrieved from the Canadian Astronomy Data Centre. MegaCam consists of 36 CCDs of 2048×4612 pixels each, with a pixel scale of $\sim 0.187''$ pixel $^{-1}$. The cluster centre is located in chip #23. The one squared degree field of view allowed a complete sampling of the cluster.

All the single WFPC2 images were reduced using the DAOPHOTIV package (Stetson 1987). In order to model the point spread function (PSF), we selected bright and

almost isolated stars in each frame. We excluded stars lying in the central regions of the PC for the $F336W$ and $F555W$ exposures, because of crowding problems. Typically ~ 200 “bona fide stars” have been used to model the PSF in the $F336W$ and $F555W$, and ~ 80 in the $F255W$. With the obtained PSF models we performed a first PSF-fitting on each single image by using ALLSTAR. Since our analysis is particularly devoted to hot stars, as master frame for the following reduction we used the stacked image obtained combining the $F336W$ and the $F255W$ exposures, using DAOMATCH/DAOMASTER/MONTAGE packages (Stetson 1994). Stars found in the master reference frame have been force-fitted to each single frame by using the ALLFRAME package (Stetson 1994). At this point we selected again the PSF stars from the ALLFRAME catalogue and we repeated the whole procedure. In this way we have minimized the risk of having spurious detections between stars used for the PSF modelling and the advantage of choosing “bona fide stars” on the basis of more reliable magnitude and improved centroid determination.

The reduction procedure for the MegaCam images is the same as for the WFPC2. In this case, however, the master list for each chip is made by stars identified in at least two out of 11 exposures. This choice allowed us to get full advantage of the dithering strategy adopted for these observations.

All the catalogues were put on the absolute astrometric system using a large number of stars in common with the Sloan Digital Sky Survey (SDSS) catalogue. As a first step we obtained the astrometric solution for each of the 36 chips of MegaCam by using the procedure described in Ferraro et al. (2001, 2003) and the cross-correlation tool CataXcorr (Montegriffo, private communication). All the stars in common with the HST field were then used as secondary astrometric standards in order to put all the catalogues in the same astrometric system. Several hundred astrometric standards have been used in each step, allowing a very precise astrometry for each catalogue. At the end of the procedure the estimated error in the absolute positions, both in right ascension (α) and declination (δ), is of about $0.2''$.

The instrumental magnitudes of the high-resolution set were corrected for charge transfer efficiency by using the equations of Dolphin (2009). All the WFPC2 magnitudes (m_{255} , m_{336} and m_{555}) were calibrated to the VEGAMAG system by using the prescription by Holtzman et al. (1995) and the zero points from the WFPC2 data handbook.¹ In order to calibrate the MegaCam magnitudes, we first transformed the g' and r' instrumental magnitudes to the SDSS system (g and r) by using the stars in common with the Sloan public catalogues. We then converted the g magnitudes in the m_{555} VEGAMAG by means of the following colour equation: $m_{555} = g - 0.501 * (g - r) + 0.256$, obtained by using the stars in common between the two catalogues.

In order to exclude extra-galactic sources from our analysis, we retrieved a catalogue of these objects from the NASA EXTRAGALACTIC DATABASE² and we matched it with our catalogues. We found a total of ~ 2880 objects

¹ <http://documents.stsci.edu/hst/wfpc2/documents/handbooks/dhb>

² <http://ned.ipac.caltech.edu/>

in common (typically galaxies and quasars) which were excluded from the following analysis.

3 CENTRE OF GRAVITY AND CMDS

Thanks to the high-resolution and quality of the WFPC2 images, we determined the centre of gravity C_{grav} of NGC 6229 from resolved stars, by following the iterative procedure described in Montegriffo et al. (1995; see also Ferraro et al. 2003, 2004; Lanzoni et al. 2007c; Dalessandro et al. 2009). We used the centre quoted by Harris (1996, 2010 version) as the first guess, and the average value of the α and δ positions of all the stars contained within circles of different radii (from $8''$ to $13''$, stepped by $1''$) as the new centre, until convergence was reached. In order to avoid possible spurious effects due to incompleteness of the catalogue, we considered three samples with different limiting magnitudes ($m_{555} = 21.0, 21.3, 21.5$). The obtained values agreed within $\sim 0.3''$, and their average was therefore assumed as C_{grav} : $\alpha(J2000.0) = 16^h 46^m 58.74^s \pm 0.28''$, $\delta(J2000.0) = 47^\circ 31' 39.53'' \pm 0.13''$. This new determination is located $\sim 0.6''$ South-West ($\Delta\alpha \simeq -0.5''$, $\Delta\delta \simeq -0.4''$) from the Harris centre.

We then used the computed cluster centre to divide the entire data set in two samples which most suitably describe different regions of the system. The *HST sample* is composed of 17307 stars measured in the WFPC2 observations and located at a distance $r < 90''$ from C_{grav} (see Figure 1). While this region is not entirely sampled by the peculiar WFPC2 field of view (FOV), according to previous work (see Sabbi et al. 2004) and in order to avoid severe incompleteness effects, we conservatively preferred to not complement this sample with low-resolution ground-based observations. The *External sample* includes all the stars measured in the MegaCam FOV at $r > 90''$, and it counts 28210 stars (see Figure 2).

The CMDs of these samples are shown in Figures 3, 4, 5. As apparent from Figure 3, the evolutionary sequences display the morphology typical of the UV plane (see Ferraro et al. 1997, 2003), with the HB crossing diagonally the diagram, the red giant branch (RGB) stars extending to colours $(m_{255} - m_{336}) \sim 6$ and always being below $m_{255} \sim 21.5$, and the BSS population defining a vertical sequence at $(m_{255} - m_{336}) \sim 0.5$, which merges without any discontinuity into the turn-off of the MS at $m_{255} \sim 22.5$. The same stars are plotted for comparison in the $(m_{555}, m_{336} - m_{555})$ plane in the left panel of Figure 4. The comparison of these two figures shows that at the optical wavelengths the cool objects (as the RGB stars) are much brighter than the hot objects (like BSS and HB stars), which instead dominate the bright portion of the CMD at UV wavelengths. For this reason, we decided to select the hot stars of the *HST sample* in the UV plane and the cool objects in the optical CMDs.

The HB of NGC 6229 has been subject of a number of studies. As suggested by Borissova et al. (1997) and Cate-lan et al. (1998) the HB morphology is characterized by a bimodal distribution in $(B - V)$ colour and shows at least one gap on the blue HB at $V \sim 18.4$. NGC 6229 is the only outer-halo cluster and one of the four known cases (the others being NGC 2808, NGC 6388 and NGC 6441) where these two anomalies are simultaneously present. Moreover, Borissova et al. (1999) identified 9 extreme HB stars in this

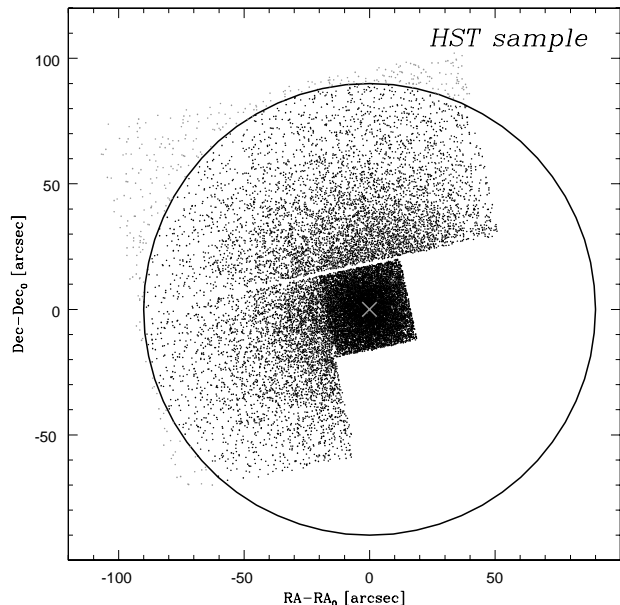


Figure 1. Map of the *HST sample*. Position of the stars measured in the WFPC2 FOV plotted with respect to the centre of gravity (large cross). The circle at $r = 90''$ marks the adopted edge of the *HST sample*.

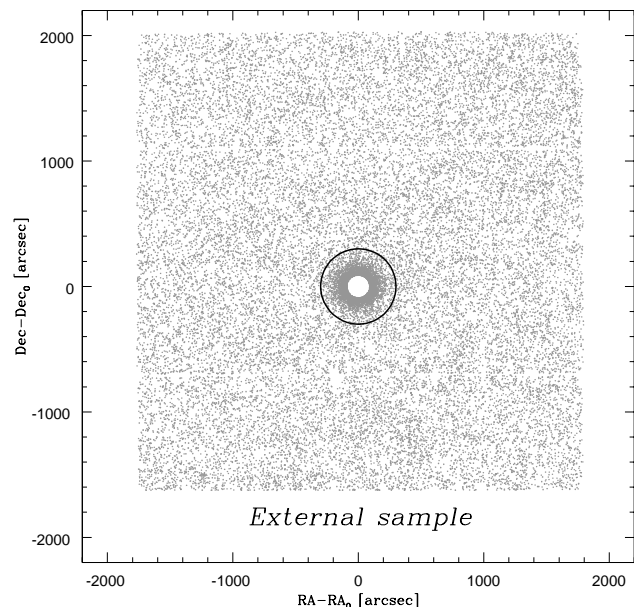


Figure 2. Map of the *External sample*. Only stars observed with MegaCam at $r > 90''$ have been included in this sample. The circle marks the nominal tidal radius of the cluster ($r = 300''$) as set by the best-fit King model shown in Figure 6.

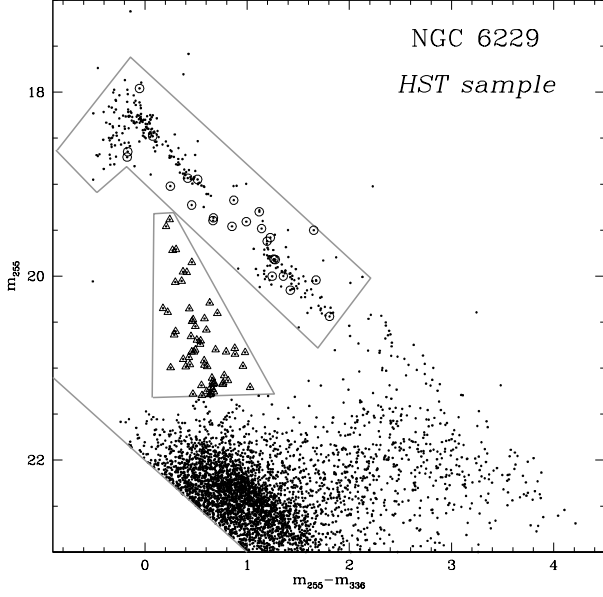


Figure 3. UV CMD of the *HST* sample. The adopted boxes used for the selection of the BSS (empty triangles) and the HB populations are shown. Known RR Lyrae stars (from Borissova et al. 2001) are marked with empty circles.

cluster. The availability of high-resolution CMDs, both in the UV and in the optical planes, clearly is a major advantage for a more detailed study of the HB morphology in NGC 6229. While this will be discussed in a forthcoming paper, here we use the HB stars only as reference population (see Section 5.2). The right panel of Figure 4 shows the $(m_{555}, m_{555} - m_r)$ CMD for the *External sample*. As can be seen, the cluster population is well defined and largely dominant over the field stars out to $r \sim 300''$. Indeed the MS of NGC 6229 can be recognized even beyond this distance (see Figure 5), while the Galactic field contamination becomes clearly dominant in the most external regions sampled by our data set.

4 RADIAL DENSITY PROFILE

We determined the projected density profile of NGC 6229 by measuring the star counts over the entire cluster extension, from C_{grav} to $r \sim 2200''$. From the *HST* sample we selected fiducial RGB, subgiant branch and bright MS stars with $19.5 < m_{555} < 21.5$. The fiducial stars are those within three times the typical photometric error from the ridge mean line of each evolutionary sequence. The same criterium was adopted to select stars from the *External sample*. In this case we considered the magnitude interval $21.0 < m_{555} < 23.0$, thus to limit the strong contamination from field stars in the most external regions, which would be particularly severe along the (scarcely populated) RGB. We divided the entire FOV in 18 annuli centred on C_{grav} and each annulus was divided into two or four subsectors, where we computed the ratio between the number of stars and the subsector area. The stellar density of each annulus is then obtained from the

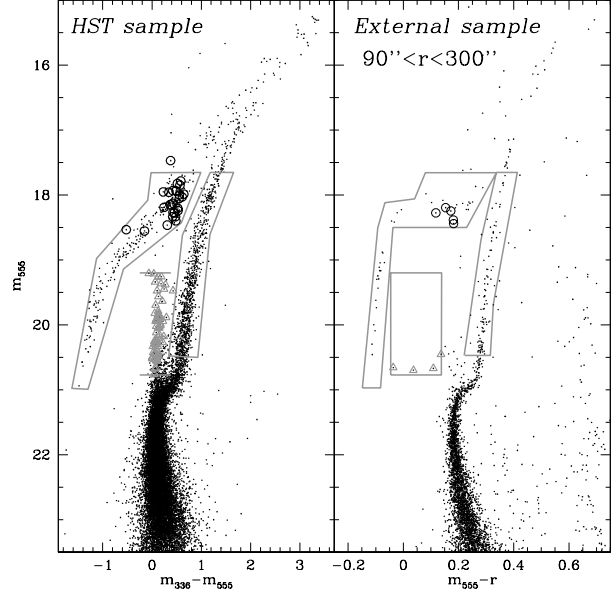


Figure 4. Optical CMDs of the *HST* and the *External* samples. The adopted selection boxes for BSS, RGB and HB stars are shown. BSS are plotted as empty triangles (those of the *HST* sample have been selected in the UV CMD shown in Figure 3). The m_{555} magnitude range for the BSS selection is also shown in the left panel by two horizontal grey segments. As in Figure 3, known RR Lyrae are marked with open circles.

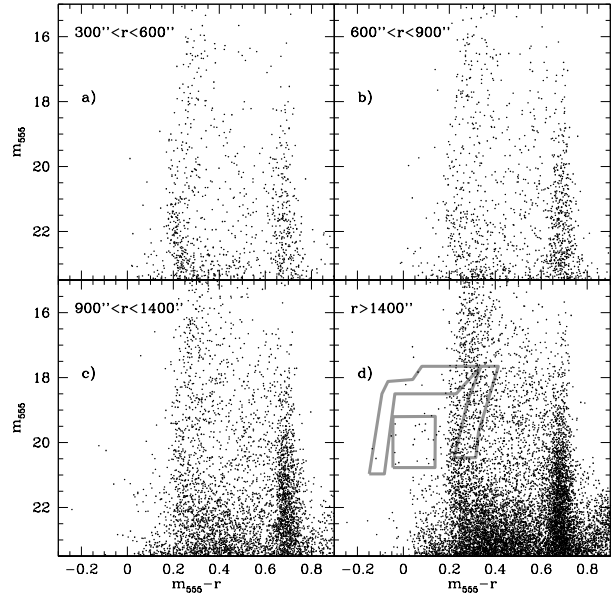


Figure 5. CMDs of the *External* sample at different radii. The cluster MS is visible (at $21 < m_{555} < 23$) even beyond the nominal cluster tidal radius ($r_t = 300''$) obtained by the best-fit King model (see Panel a). Panel d) shows the region used to determine the field star contamination; the adopted selection boxes for BSS, RGB and HB stars are also marked.

average of the corresponding subsector densities and the errors from the squared root of their variance. The incomplete area coverage affecting some annulus has been taken into account in this procedure. In order to join the star counts in the inner and outer regions, we determined the density of the *External sample* in the annulus $60'' < r < 90''$ using the same magnitude range adopted for the *HST sample* ($19.5 < m_{555} < 21.5$) and we used this point to normalize the two distributions. The resulting radial density profile is shown in Figure 6. The last three points ($r > 750''$) have been used to estimate the contribution of the background stars.

The single mass King model that best fits the observed density profile (see the solid line on figure) has concentration $c \simeq 1.49$ and core radius $r_c \simeq 9.5''$. These values are consistent with those ($c = 1.50$, $r_c = 7.7''$) quoted by McLaughlin & van der Marel (2005), who however fit the surface brightness (instead of the surface density) profile, only out to $r \sim 100''$. Our fit well reproduces the central part of the profile and confirms that NGC 6229 has not experienced the collapse of the core yet, as suggested by Djorgovski & King (1986), Trager et al. (1995), Borissova et al. (1997). However, neither our best-fit model, nor those found in the literature are able to properly reproduce the external density profile (see the figure). In fact, the best-fit King model systematically underpredicts the number counts for $r > 250''$ and a prominent MS belonging to the cluster is well appreciable beyond the nominal tidal radius of the model, set at $r \sim 300''$ (see Figure 5). This discrepancy requires a more detailed investigation, which is out of the scope of the present paper.

5 THE BSS POPULATION

5.1 The BSS selection

For the *HST sample* we selected the BSS population in the $(m_{255}, m_{255} - m_{336})$ diagram. The adopted selection box is shown in Figure 3. In order to avoid the contamination from MS turn-off stars, we limit the sample to $m_{255} < 21.3$. Within this threshold, we identify 60 BSS in the *HST sample*, which are also shown in the left panel of Figure 4 and turn out to span the magnitude range $19.2 < m_{555} < 20.75$. Because of the quality of the optical CMD, the BSS selection in the *External sample* is quite straightforward. We used the same magnitude limits inferred in the optical plane by stars selected in the UV, while the extension in colour has been set by the four candidate BSS visible in this diagram at $-0.05 < (m_{555} - r) < 0.15$. The selection box is shown in grey in the figure. Interestingly enough the most external BSS lies at $\sim 130''$ from the centre, i.e. well within the cluster tidal radius. Thus the final sample of BSS counts 64 objects in the surveyed region of the cluster.

A preliminary study of the BSS population at $r > 32''$ has been presented by Borissova et al. (1999), using optical ground-based data. It is not possible to compare that sample with our much higher resolution HST data covering the central and most crowded region of the cluster. However, when comparing the ground-based data in the outskirts of the cluster, we find that the number (4) of BSS at $r > 90''$ in the *External sample* is in good agreement with the number (5) quoted by Borissova et al. (1999).

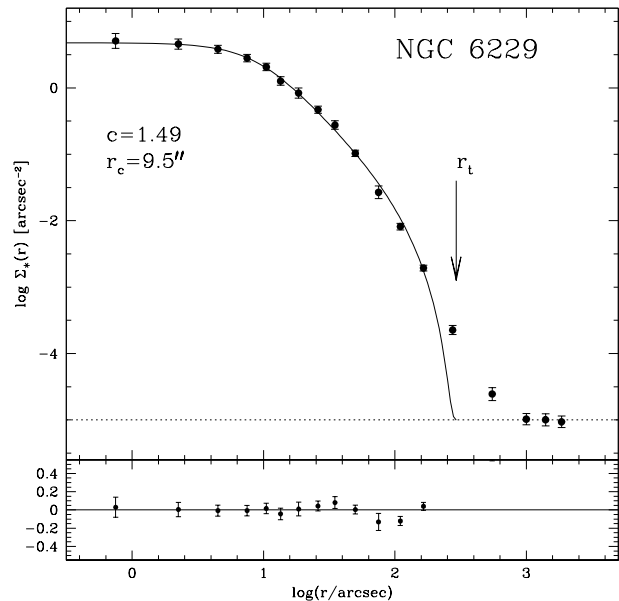


Figure 6. Observed surface density profile (filled circles) and best-fit King model (solid line). The radial profile is in unit of number of stars per square arcsecond. The dotted line indicates the adopted level of the background, computed as the average of the three outermost points. The location of the nominal cluster tidal radius is marked by the arrow. The lower panel shows the residuals between the observations and the fitted profile for $r \leq 200''$.

5.2 The reference populations

As already discussed in other papers (see e. g. Ferraro et al. 1995, 1997) in order to study the BSS properties, we need to select also a reference population representative of the normal cluster stars. To this end, we consider both the HB and the RGB populations. Since the HB of NGC 6229 is bimodal (Borissova et al. 1997; Catelan et al. 1998) and it is populated by stars cooler and hotter than the instability strip, we decided to select HB stars by using both the UV and the optical planes, when possible. In fact the $(m_{255}, m_{255} - m_{336})$ guarantees a solid selection of the blue HB stars, while it is strongly incomplete for stars with $(m_{255} - m_{336}) > 2.5$, which are instead among the brightest objects in the optical plane. We first selected HB stars in the UV plane by using the selection box shown in Figure 3. Thanks to the adopted photometric reduction method, all the stars selected in this way are also identified in the $(m_{555}, m_{336} - m_{555})$ plane and they lie at $(m_{336} - m_{555}) < 0.5$. We then built a selection box in the optical CMD including both the stars identified in the UV and the HB stars redder than $(m_{336} - m_{555}) = 0.5$ (see left panel of Figure 4). This selection allows us to identify all the HB stars and to obtain the magnitude limits for the selection in the outermost regions of the cluster. In fact, since no UV filters are available for the *External sample*, we selected HB stars in the $(m_{555}, m_{555} - r)$ CMD by using the same magnitude limits ($17.5 < m_{555} < 21.0$) used in the optical CMD of the *HST sample*. All the 30 known RR Lyrae stars at $r > 15''$ (Borissova et al. 2001) located in our FOV have been included in the HB selection. Consid-

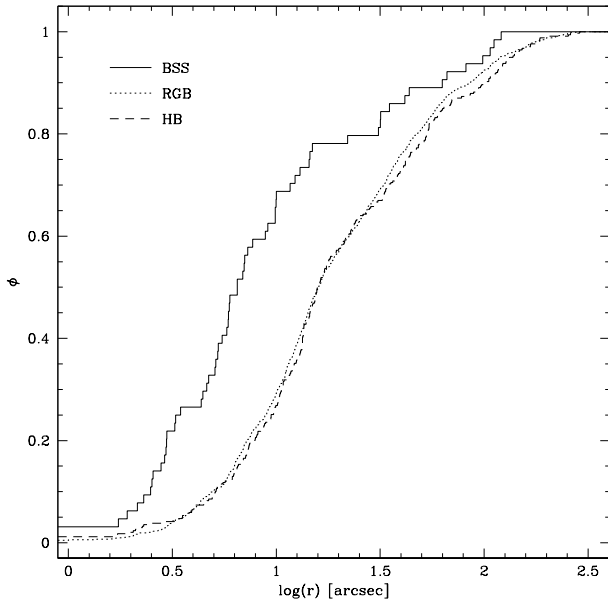


Figure 7. Cumulative radial distribution of BSS (solid line), HB (dashed line) and RGB (dotted line) stars as a function of the projected distance from C_{grav} .

ering the entire FOV, from C_{grav} to $r \sim 300''$, we identify 339 HB stars, 299 in the *HST* sample and 40 in the *External* sample. To select the RGB stars we used the optical CMDs, where these objects are bright and the branch well defined. In order to reduce the contamination from subgiant and asymptotic giant branch stars, we limit our selection to $17.5 < m_{555} < 20.5$. We identify 1027 RGB stars, 930 in the *HST* field and 97 in the *External* field. The boxes adopted to identify the reference populations are shown in both panels of Figure 4.

5.3 The BSS radial distribution

Figure 7 shows the cumulative radial distribution for the three selected populations (namely BSS, HB and RGB). As evident, BSS are more centrally concentrated than the others. The Kolmogorov-Smirnov (K-S) test gives a probability of $\sim 7 \times 10^{-9}$ and $\sim 6 \times 10^{-9}$ that BSS are extracted from the same parent populations of RGB and HB stars, respectively.

For a more quantitative analysis, we computed the population ratios N_{BSS}/N_{HB} , N_{BSS}/N_{RGB} and N_{HB}/N_{RGB} in seven concentric annuli centred in C_{grav} . In order ensure that our results are not affected by severe field contamination, we carefully evaluated the expected number of field stars in each selection box. To this end we exploit the huge FOV covered by the MegaCam catalogue, that allows us to statistically quantify the contamination of the field stars well beyond $r = 300''$. In particular we used the CMD obtained for $r > 1400''$, where field stars define two vertical sequences roughly located at $0.2 < (m_{555} - r) < 0.4$ and $0.5 < (m_{555} - r) < 0.8$. By counting the number of stars lying within the boxes used for the population selections, we derived the following values for the field star densities: $\rho_{BSS} \sim 0.010$ stars arcmin $^{-2}$, $\rho_{HB} \sim 0.027$ stars

r''_i	r''_e	N_{BSS}	N_{HB}	N_{RGB}
0	5	21	33	105
5	15	29	125	385
15	35	4	80	251
35	60	3	46	136
60	90	3	15	53
90	130	4	21	53 (1)
130	300	0	19 (2)	44 (7)

Table 1. Number of BSS, HB and RGB stars counted in the seven concentric annuli used to study the BSS radial distribution. The values in parenthesis are the estimated number of contaminating field stars in each annulus (see text, Section 4.2).

arcmin $^{-2}$, $\rho_{RGB} \sim 0.102$ stars arcmin $^{-2}$. This indicates that the BSS and the HB samples are not very affected by field stars contamination within $300''$. Indeed, after the decontamination from field stars, we obtain $N_{BSS} = 64$, $N_{HB} = 337$, $N_{RGB} = 1019$, and a total specific frequency of BSS $F_{HB}^{BSS} = N_{BSS}/N_{HB} \simeq 0.19$.

The star counts for each annulus are listed in Table 1 and have been used to compute the population ratios as a function of the radial distance from the cluster centre (see Figure 8). The BSS distribution is clearly bimodal, with a high peak in the centre, a minimum at $r \sim 40''$ and a rising branch in the outer region. In contrast, the N_{HB}/N_{RGB} ratio (bottom panel of the figure) is flat across the entire extension of the cluster, as expected for normal, not segregated populations. The central segregation of BSS is quite high. In fact, $\sim 67\%$ of the entire BSS sample is located within $r \leq 10''$, while only $\sim 27\%$ of the reference stars is found in the same region. By assuming the central luminosity density quoted by Harris (1996, 2010 version) and the central velocity dispersion (6.8 km s $^{-1}$) published by McLaughlin & van der Marel (2005), the resulting radius of avoidance (see e. g. Mapelli et al. 2006) would be $r_{av} \simeq 75''$. This value is larger than the observed position of the minimum of the radial distribution. However, we note that a (reasonably larger) velocity dispersion of ~ 9 km s $^{-1}$ would be sufficient to bring into agreement these two quantities. In addition, in such a computation we are assuming a King model that underestimates the cluster density in the outer regions, and this could also be responsible for at least part of the discrepancy. Since a more precise analysis is not possible at the moment we can only conclude that the central regions of NGC 6229 likely are already relaxed, while its outskirts still are not much affected by dynamical friction effects.

6 SUMMARY

In this paper we have used a combination of HST UV and optical images of the cluster centre, and wide-field ground-based optical observations covering the entire cluster extension to derive the main structural parameters of the globular cluster NGC 6229 and to study its BSS population.

From the high-resolution data we derived the cluster centre of gravity lying at $\alpha(J2000.0) = 16^h 46^m 58.74^s$, $\delta(J2000.0) = 47^\circ 31' 39.53''$, with an uncertainty of $\sim 0.3''$ in both α and δ . We determined the radial density profile from star counts, finding that the King model that best fits

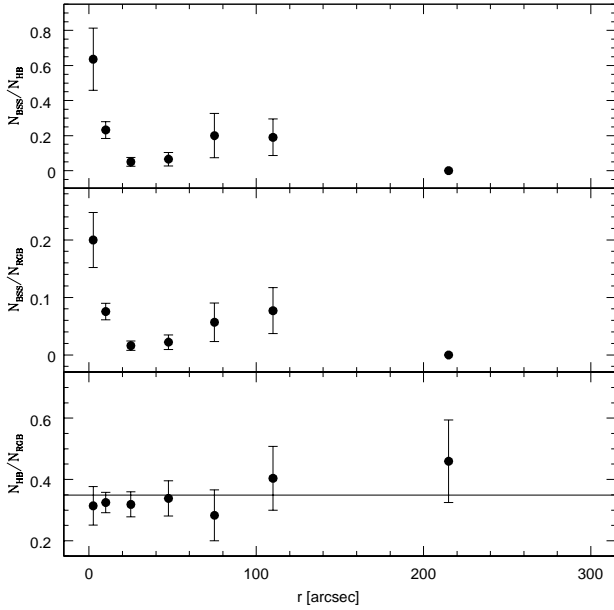


Figure 8. Distribution of the population ratios $N_{\text{BSS}}/N_{\text{HB}}$, $N_{\text{BSS}}/N_{\text{RGB}}$, $N_{\text{HB}}/N_{\text{RGB}}$ (top, middle, bottom, respectively) as a function of the radial distance from the cluster centre.

the central region (out to $\sim 250''$) is characterized by a core radius $r_c \simeq 9.5''$ and a concentration $c \simeq 1.49$. However such a model does not well reproduce the outermost portion of the cluster profile.

A total of 64 BSS (60 in the *HST* sample and 4 in the *External* sample) has been identified. The radial distribution of BSS with respect to normal cluster stars (HB and RGB) is bimodal: with a high peak in the centre, a clear-cut dip at intermediate radii ($\sim 40''$), and an upturn in the external regions. Such a bimodality is quite similar to that found in the majority of the GCs investigated so far, and it has been interpreted as the result of the dynamical relaxation of the clusters (e. g. Beccari et al. 2008; Dalessandro et al. 2009; see also Section 1).

ACKNOWLEDGMENTS

This research used the facilities of the Canadian Astronomy Data Centre operated by the National Research Council of Canada with the support of the Canadian Space Agency. This research is part of the project COSMIC-LAB founded by the European Research Council (under contract ERC-2010-AdG-267675). Financial contribution of the Italian Istituto Nazionale di Astrofisica (INAF, under contract PRIN-INAF 2008) and the Agenzia Spaziale Italiana (under contract ASI/INAF/I/009/10) is also acknowledged. The research leading to these results has received funding also from the European Community's Seventh Framework Programme (/FP7/2007-2013/) under grant agreement No 229517.

REFERENCES

- Beccari, G., et al. 2008, *ApJ*, 679, 712
- Beccari, G., Sollima, A., Ferraro, F. R., Lanzoni, B., Bellazzini, M., De Marchi, G., Valls-Gabaud, D., Rood, R. T. 2011, *ApJ Letters*, 737, 3
- Borissova, J., Catelan, M., Spassova, N., Sweigart, A. V. 1997, *AJ*, 113, 692
- Borissova, J., Catelan, M., Ferraro, F. R., Spassova, N., Buonanno, R., Iannicola, G., Richtler, T., Sweigart, A. V. 1999, *A&A*, 343, 813
- Borissova, J., Catelan, M., Valchev, T. 2001, *MNRAS*, 324, 77
- Catelan, M., Borissova, J., Sweigart, A. V., & Spassova, N. 1998, *ApJ*, 494, 265
- Contreras Ramos, R., Ferraro, F. R., Dalessandro E., Lanzoni, B., Rood, R. T. 2012, *arXiv:astro-ph/1201.4959*
- Dalessandro, E., Lanzoni, B., Ferraro, F. R., Rood, R. T., Milone, A., Piotto, G., & Valenti, E. 2008a, *ApJ*, 677, 1069
- Dalessandro, E., Lanzoni, B., Ferraro, F. R., Vespe, F., Bellazzini, M., & Rood, R. T. 2008b, *ApJ*, 681, 311
- Dalessandro, E., Beccari, G., Lanzoni, B., Ferraro, F. R., Schiavon, R., & Rood, R. T. 2009, *ApJ*, 182, 509
- Djorgovski, S., King, I. R. 1986, *ApJ*, 305, 61
- Dolphin, A. E. 2009, *PASP*, 121, 655
- Ferraro, F. R., Fusi Pecci, F., Bellazzini, M. 1995, *A&A*, 294, 80
- Ferraro, F. R., Paltrinieri, B., Fusi Pecci, F., Cacciari, C., Dorman, B., Rood, R. T., Buonanno, R., Corsi, C. E., Burgarella, D., & Laget, M. 1997, *A&A*, 324, 915
- Ferraro F. R., Messineo M., Fusi Pecci F., De Palo M. A., Straniero O., Chieffi A., & Limongi M. 1999, *AJ*, 118, 1738
- Ferraro, F. R., D'Amico, N., Possenti, A., Mignani, R. P., & Paltrinieri, B. 2001, *ApJ*, 561, 337
- Ferraro, F. R., Sills, A., Rood, R. T., Paltrinieri, B., & Buonanno, R. 2003, *ApJ*, 588, 464
- Ferraro, F. R., Beccari, G., Rood, R. T., Bellazzini, M., Sills, A., & Sabbi, E. 2004, *ApJ*, 603, 127
- Ferraro, F. R., et al. 2006a, *ApJ*, 647, L53
- Ferraro, F. R., Sollima, A., Rood, R. T., Origlia, L., Pancino, E., & Bellazzini, M. 2006b, *ApJ*, 638, 433
- Ferraro, F. R., Beccari, G., Dalessandro, E., Lanzoni, B., Sills, A., Rood, R. T., Pecci, F., Fusi, Karakas, A. I., Miocchi, P., Bovinelli, S. 2009, *Nature*, 462, 1028
- Harris, W.E. 1996, *AJ*, 112, 1487
- Holtzman, J. A., Burrows, C. J., Casertano, S., Hester, J. J., Trauger, J. T., Watson, A. M., & Worthey, G. 1995, *PASP*, 107, 1065
- Lanzoni, B., Dalessandro, E., Ferraro, F. R., Mancini, C., Beccari, G., Rood, R. T., Mapelli, M., & Sigurdsson, S. 2007b, *ApJ*, 663, 267
- Lanzoni, B., Sanna, N., Ferraro, F. R., Valenti, E., Beccari, G., Schiavon, R. P., Rood, R. T., Mapelli, M., & Sigurdsson, S. 2007a, *ApJ*, 663, 1040
- Lanzoni, B., Dalessandro, E., Ferraro, F. R., Miocchi, P., Valenti, E., & Rood, R.T. 2007c, *ApJ*, 668, L139
- Mapelli, M., Sigurdsson, S., Colpi, M., Ferraro, F. R., Possenti, A., Rood, R. T., Sills, A., & Beccari, G. 2004, *ApJ*, 605, L29
- Mapelli, M., Sigurdsson, S., Ferraro, F. R., Colpi, M., Possenti, A., & Lanzoni, B. 2006, *MNRAS*, 373, 361
- McCrea, W. H. 1964, *MNRAS*, 128, 147
- McLaughlin, D. E., & van der Marel, R. P. 2005, *ApJs*, 161, 304
- Montegriffo, P., Ferraro, F. R., Fusi Pecci, F., & Origlia, L. 1995, *MNRAS*, 276, 739
- Palma, C., Majewski, S. R., Johnston, K. V. 2002, *ApJ*, 564, 736
- Pietrinferni, A., Cassisi, S., Salaris, M., & Castelli, F. 2004, *ApJ*, 612, 168
- Sabbi, E., Ferraro, F. R., Sills, A., & Rood, R. T., 2004, *ApJ* 617, 1296
- Shara, M. M., Saffer, R. A., & Livio, M. 1997, *ApJ*, 489, L59
- Sills, A., Lombardi, J. C. Jr., Bailyn, C. D., Demarque, P., Rasio, F. A., Shapiro, S. L. 1997, *ApJ*, 487, 290

Stetson, P. B. 1987, PASP, 99, 191

Stetson, P. B. 1994, PASP, 106, 250

Trager, S. C., King, I. R., Djorgovski, S. 1995, AJ, 109, 218